ACS APPLIED MATERIALS & INTERFACES

Research Article

Cite This: ACS Appl. Mater. Interfaces 2019, 11, 48612−48623

www.acsami.org

Boron-Doped Nanocrystalline Diamond−Carbon Nanospike Hybrid Electron Emission Source

Kamatchi Jothiramalingam Sankaran,*[,†,‡] Mateusz Ficek,[§] Kalpataru Panda,[∥,⊥] Chien-Jui Yeh,[#] Miroslaw Sawczak,[¶] Jacek Ryl,[▽] Keh-Chyang Leou,[#] Jeong Young Park,[∥,⊥] I-Nan Lin,[○] Robert Bogdanowicz,[§] and Ken Haenen*[,†,‡]

[†]Institute for Materials Research (IMO), Hasselt University, 3590 Diepenbeek, Belgium

[‡]IMOMEC, IMEC vzw, 3590 Diepenbeek, Belgium

[§]Department of Metrology and Optoelectronics, Faculty of Electronics, Telecommunications and Informatics, Gdansk University of Technology, 11/12 G. Narutowicza Street, 80-233 Gdansk, Poland

[∥]Center for Nanomaterials and Chemical Reactions, Institute for Basic Science (IBS), 34141 Daejeon, Korea

[⊥]Department of Chemistry, Korea Advanced Institute of Science and Technology (KAIST), 34141 Daejeon, Korea

[#]Department of Engineering and System Science, National Tsing Hua University, Hsinchu, 30013 Taiwan, Republic of China

[¶]Center for Plasma and Laser Engineering, The Szewalski Institute of Fluid Flow Machinery, Polish Academy of Sciences, Fiszera 14, 80-231 Gdansk, Poland

[▽]Department of Electrochemistry, Corrosion and Materials Engineering, Faculty of Chemistry, Gdansk University of Technology, Narutowicza 11/12, 80-233 Gdansk, Poland

[○]Department of Physics, Tamkang University, Tamsui, 251 Taiwan, Republic of China

Supporting Information

ABSTRACT: Electron emission signifies an important mechanism facilitating the enlargement of devices that have modernized large parts of science and technology. Today, the search for innovative electron emission devices for imaging, sensing, electronics, and high-energy physics continues. Integrating two materials with dissimilar electronic properties into a hybrid material is an extremely sought-after synergistic approach, envisioning a superior field electron emission (FEE) material. An innovation is described regarding the fabrication of a nanostructured carbon hybrid, resulting from the one-step growth of boron-doped nanocrystalline diamond (BNCD) and carbon nanospikes (CNSs) by a microwave plasma-enhanced chemical vapor deposition technique. Spectroscopic and microscopic tools are used to investigate the morphological, bonding, and microstructural characteristics related to the growth mechanism of these hybrids. Utilizing the benefits of both the sharp edges of the CNSs and the high stability of BNCD, promising FEE performance with a lower turn-on field of 1.3 V/μm, a higher field enhancement factor of 6780, and a stable FEE current stability lasting for 780 min is obtained. The microplasma devices utilizing these hybrids as a cathode illustrate a superior plasma illumination behavior. Such hybrid carbon nanostructures, with superb electron emission characteristics, can encourage the enlargement of several electron emission device technologies.

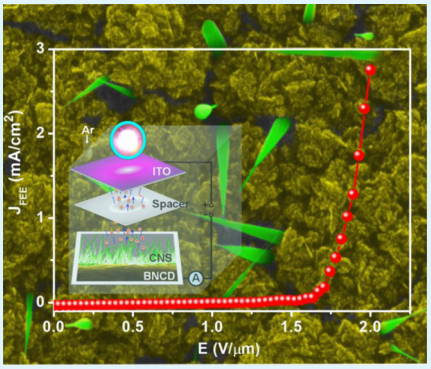

KEYWORDS: *nanocrystalline diamond, carbon nanospike, one-step growth, field electron emission, microplasma illumination*

INTRODUCTION

Modernization of novel electron sources is essential for numerous applications comprising integrated flat panel displays, electron guns, vacuum microelectronics, X-ray sources, and energy conversion devices. Field electron emission (FEE)-based electron sources, specifically "cold-cathodes", are replacing conventional thermionic electron emission sources. FEE, also well known as Fowler−Nordheim (F−N) tunneling,[1] follows a quantum tunneling mechanism, where under an external electric field, electrons pass from a material's surface into a vacuum. For choosing a suitable material as an effective field emitter cathode, numerous standards such as high chemical and mechanical stability, vacuum compatibility, electron affinity, resistance to poisoning because of residual gases and ion bombardment, are considered.

Owing to the fact that physical and geometrical parameters are greatly responsible for the electron tunneling characteristics, one-dimensional (1D) nanostructures, for example,

Received: October 8, 2019
Accepted: December 3, 2019
Published: December 3, 2019

DOI: 10.1021/acsami.9b17942
ACS Appl. Mater. Interfaces 2019, 11, 48612−48623

nanotubes, nanowires, and nanorods have been deliberated as favorable emitter materials for FEE devices. For overcoming the disadvantages of bulk device technologies, 1D nanostructures have quicker device turn-on time, sustainability, and compactness. Additionally, long and sharp nanoneedles pointing in the various directions of these nanostructures are promising for improving the FEE current density. A myriad of nanostructures from metals, semiconductors, and carbon materials has been developed in an attempt to achieve better FEE performance, including Ge, Cu and Au nanowires, SiC nanoparticles, PrB_6 nanorods, WS_2 nanotubes, ZnO nanowalls, graphene nanoedges, boron nanosheets, carbon nanotubes (CNTs), diamond nanorods, and many others.[2−11] Compared to metals and semiconductors, carbon nanostructures such as CNTs, carbon nanosheets, nanodiamonds, and graphene show enhanced FEE characteristics.[12]

Generally, materials with outstanding FEE characteristics display a low turn-on field, high current density, large field enhancement factor, high stability, and long lifetime. However, it is very hard to discover these characteristics in a single material. For example, along with the sharp edges and high aspect ratio, CNTs and graphene create a low turn-on field, high current density, and high field enhancement factor. Nevertheless, these materials face the challenges of insufficient device lifetime and long-term emission stability.[13,14] The FEE properties of these materials are degraded because the residual gases in the FEE devices damage the sharp edges of these materials after a long-time ion bombardment. On the other hand, because of its strong bonding structure, diamond shows better lifetime stability and reliability, but its intrinsic insulating nature results in a high turn-on field and low current density. Consequently, combining different nanoscale carbon materials to synthesize a hybrid material is considered to be an effective route to achieve enhanced FEE characteristics compared with a single nanocarbon material. Varshney et al. have fabricated a layered graphene−diamond hybrid that achieves a turn-on field of 3.8 V/μm and a long-lasting stable FEE current of 0.1 mA over 135 h.[15] CNTs−carbon nanoflake hybrid balls with a low turn-on field of 1.77 V/μm were successfully synthesized by Chang et al.[16] Microcrystalline diamond/CNT double-layered pyramid arrays acquire a low turn-on field of 2.84 V/μm and a long lifetime above 100 h.[17] Chang et al. have coated nitrogen-doped diamond on CNTs that display a low turn-on field of 3.58 V/μm and noticeably improved the robustness of CNTs.[18] Yuge et al. described a low turn-on field of 12 kV cm^{-1} for single-walled CNTs grown on single-walled carbon nanohorn aggregates.[19] Graphene/carbon nanofilament hybrids illustrate a low turn-on field of 1.34 V/μm and a high field enhancement factor of 4930, which were reported by Dai et al.[20] Xiao et al. developed an ultrananocrystalline diamond−carbon nanofiber hybrid field emitter with a low threshold field emission of 2.5 V/μm.[21] FEE tests of microstructured diamond films/vertically aligned multiwalled CNT reveal low threshold voltages of 2 V/μm with longer lifetime stability up to 35[22] and 75 h.[23] Uppireddi et al. synthesized hybrid films comprising microstructured diamond film carbon nanostructures, which showed low turn-on field of 2.5 V/μm and good temporal stability over a period of 24 h.[24] Hybrid graphene−CNT field emitters reported by Koh et al.[25] and Liu et al.[26] show lower turn-on field, which is ascribed to the enhanced electrical conductivity and field enhancing emission spots on the surface of the graphene sheet. Also, a hybrid film with a reduced graphene oxide−CNT reveals a low turn on field and threshold field of 2.82 and 3.00 V/μm, respectively.[27] Catalytically synthesized few-layer graphene on vertically aligned diamond nanorods shows a low turn-on field of 4.21 V/μm and a large field enhancement factor of 3480.[28] However, a multistep growth process is involved in fabricating these hybrids materials, which are technologically complicated and more economically unfavored.

In this work, a direct one-step microwave plasma enhanced chemical vapor deposition (MPECVD) synthesis of boron-doped nanocrystalline diamond (BNCD)−carbon nanospike (CNS) hybrids is presented, with CNS-on-BNCD as the key motivation. The BNCD−CNS hybrids are outstanding field electron emitters with all of the preferred characteristics, such as low turn-on field, high field enhancement factor, and prolonged emission stability, which are superior to those of other kinds of hybrids reported earlier. The atomic force microscopy (AFM)-based peak forced-tunneling AFM (PF-TUNA) technique was used to directly explore the local electron emission sites from these hybrids. Moreover, the potential applications of these superior FEE hybrid materials as microplasma cathodic devices were demonstrated.

RESULTS AND DISCUSSION

Material's Characteristics. Scanning electron microscopy (SEM) was employed to examine the BNCD−CNS hybrids. The cross-sectional SEM micrograph shown in Figure 1a reveals that 1D separated spike-shaped carbon nanostructures were grown directly on the BNCD films. The nanospikes are sharp, vertically aligned, and no branching was observed; they are distributed randomly on the whole surface of the BNCD films. The size of the CNSs was estimated to be ∼50−100 nm in diameter and ∼2 μm in height. Figure 1b shows the plan-view SEM image which exhibits that CNSs were protruding

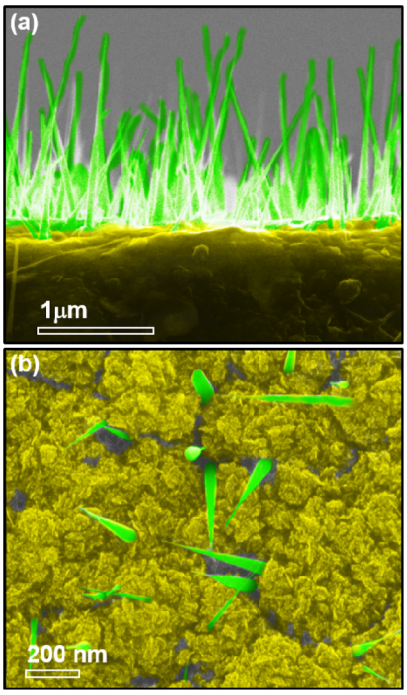

Figure 1. (a) Cross-sectional SEM micrograph of BNCD−CNS hybrids and (b) corresponding plan-view SEM micrograph. The SEM micrographs of BNCD samples after first phase of growth are presented in Figure S1, Supporting Information.

DOI: 10.1021/acsami.9b17942
ACS Appl. Mater. Interfaces 2019, 11, 48612−48623

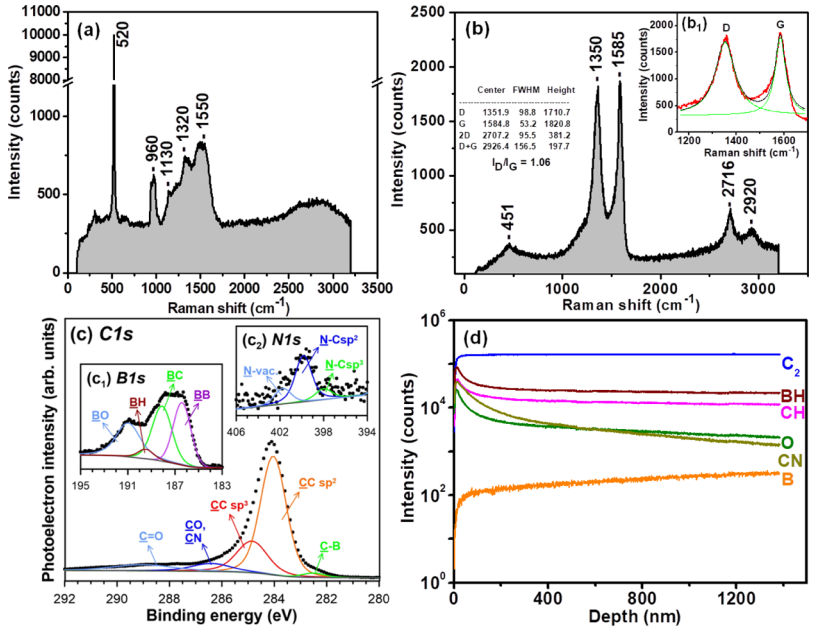

Figure 2. Visible-Raman (λ = 514 nm) spectra of (a) BNCD and (b) BNCD−CNS hybrids. The full-width half maximum and intensities of D and G bands of BNCD−CNS hybrids, determined by fitting with a Lorentzian distribution, are shown in the inset b_1. (c) C 1s XPS spectrum of BNCD−CNS hybrids along with B 1s [inset (c_1)] and N 1s [inset (c_2)] XPS spectra of the materials. (d) SIMS depth profile of the growth species such as C_2, BH, CH, CN, and B in the $H_2/CH_4/B_2H_6/N_2$ plasma.

outside from the BNCD films and the BNCD films have 10−20 nm sized cauliflower-like grains with thickness around 1.2 μm. Moreover, Figure S1a of the Supporting Information displays the SEM micrograph of a thin layer of BNCD films grown directly on a silicon substrate in the first stage of the sample preparation. The thickness of thin BNCD films is around 170 nm, which is estimated from the cross-sectional SEM micrograph shown in Figure S1b, Supporting Information.

Raman and X-ray photoelectron spectroscopy (XPS) measurements were accomplished to understand the chemical bonding states of the BNCD−CNS hybrids. The Raman spectrum shown in Figure 2a was recorded for a thin layer of BNCD grown directly on a silicon substrate in the first stage of the sample preparation. Except for the silicon bands at 520 and 960 cm^{-1}, the wide band with maximum around 1320 cm^{-1} is observed, which is due to the nanocrystalline features of diamond grains in the BNCD films (cf. Figure 1b).[19] Generally, a sharp Raman peak at 1332 cm^{-1} is observed for the diamond films with large grain sizes.[13,28] The ν_1 band at ~1130 cm^{-1} reveals the presence of *trans*-polyacetylene phases at the grain boundaries (GB).[29] The band at 1550 cm^{-1} represents the G band (sp^2 carbon phase). The Raman spectrum recorded for the BNCD−CNS hybrids shown in Figure 2b is different from the Raman spectrum observed for the first stage of BNCD film growth (cf. Figure 2a). The spectrum is dominated by two intense bands: the D band centered near 1350 cm^{-1} is initiated by the lattice disorder ensuing from the finite crystalline size and the G band centered near 1585 cm^{-1} signifies the presence of E_{2g} mode of graphite,[30] respectively. The peak positions, full-width half maximum, and intensities of the D and G bands, determined by fitting a Lorentzian distribution are listed in inset b_1 of Figure 2b. The I_D/I_G ratio for the investigated material is 1.06, which corresponds to a multiwalled CNT-like structure.[31] A second-order two-dimensional (2D) band arises around 2716 cm^{-1}, signifying the presence of nanographite and a D + G band at 2920 cm^{-1} is due to defects at sp^2 sites. Besides this, in the low wavenumber range, a wide asymmetric band with a maximum at 451 cm^{-1} was noticed, indicating boron-doped carbon materials originating in boron-induced defects.

The XPS analysis was performed in the binding energy range characteristic for C 1s, B 1s, and N 1s, as presented in Figure 2c. The dominant influence of carbon was revealed, with five individual components present in the C 1s spectrum. Most notably, two peaks located at 284.0 and 284.8 eV are related to sp^2 and sp^3 carbon, respectively. The sp^2-to-sp^3 ratio, estimated on the basis of XPS data analysis was found to be 2.9:1. Next, two carbon components were located at more positive energies, corresponding to oxidized C−O and C−N bonds. The incorporation of boron into a nanospike lattice is indicated by the appearance of a peak at 282.5 eV.[32] In the B 1s region (inset c_1 of Figure 2c), the broad peak shape indicates the presence of multiple types of boron interactions. The majority of the absorption peaks are observed to be associated with elemental boron and B−C bonding energies.[33] The small contribution at 189.5 eV reveals the presence of B−H bonds. A similar interaction was previously observed in the case of borohydrides.[34] However, similar peak energies were reported for a boron atom substituted in the graphitic structure.[35] Next, the B 1s peak value of 191.0 eV shows the sign of boron oxidation in the analyzed sample. The presence of oxygen on the sample surface originated from exposure to the atmosphere, and its contribution did not exceed 5%, a value typical for air-exposed diamond-based electrodes.[36] On the other hand, inset c_2 of Figure 2c shows the deconvoluted N 1s spectrum. The dominant component at 399.9 eV is ascribed to nitrogen atoms in the sp^2 carbon environment, while the component attributed to nitrogen atoms bonded with sp^3 carbon is typically shifted to more negative binding energies, here, at 398.0 eV. Their ratio corresponds to the sp^2-to-sp^3 ratio obtained based on C 1s spectrum deconvolution. Finally,

DOI: 10.1021/acsami.9b17942
ACS Appl. Mater. Interfaces 2019, 11, 48612−48623

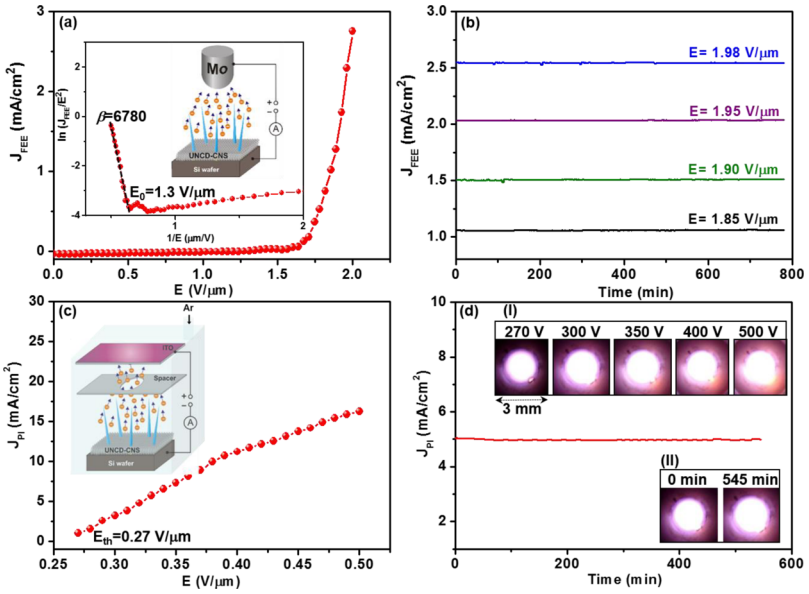

Figure 3. (a) FEE current density (J_{FEE}) as a function of applied field (E) for BNCD−CNS hybrids with the inset showing the F−N corresponding J_{FEE}−E characteristic curve along with the turn-on field (E_0 = 1.3 V/μm) and the schematic of the FEE measurement. (b) Lifetime stability test, J_{FEE} vs time curve, for hybrids at different applied fields. (c) Plasma current density (J_{PI}) vs applied field (E) of a microplasma cavity, which utilized ITO-coated glass as the anode and BNCD−CNS hybrids as the cathode materials. The inset of (c) shows the schematic of the PI measurement setup along with the threshold field (E_{th} = 0.27 V/μm). (d) PI stability of the BNCD−CNS hybrids. Inset (I) shows the photographs of the PI characteristics of the microplasma devices at varying voltages, and inset (II) shows the PI intensity at 0 and 545 min after ignition of the plasma, revealing that the plasma device essentially did not degrade even after long service time.

the most positively charged nitrogen atoms originate from surface contamination with oxygen or nitrogen atoms trapped in vacancy defects created in the nitride layer. The deconvolution results are summarized in Table S1, Supporting Information. The induction of sp^2 phases in BNCD−CNS hybrids because of B and N doping discloses that doping of heteroatoms in carbon increases the graphitic nature as well as the electrical conductivity.[37,38] Furthermore, secondary ion mass spectroscopic (SIMS) measurements were carried out to confirm the elemental species assisting in the formation of BNCD−CNS hybrids. The SIMS depth profile of the growth species such as C_2, BH, CH, CN, and B is displayed in Figure 2d, whereas the corresponding 2D mapping is shown in Figure S2. We clearly observed that the C_2 species possess a high intensity with high bright regions (Figure S2a). BH and CH species are almost at the same intensity followed by the CN, O, and B species, which indicates a uniform distribution of these species throughout the thickness of the films. This is contradictory to the common observation that boron concentration is usually present at the surface rather than throughout the bulk of the material.[39] The SIMS depth profile is consistent with the observations from the XPS studies.

Potential Applications. *Field Electron Emitters.* Various functional properties can be envisioned from these hybrid materials. Owing to their sharply pointed 1D nanospikes, these hybrids are anticipated to be an effective field electron emitter. Figure 3a shows the FEE plot of the current density (J_{FEE}) as a function of the applied electric field (E) for the BNCD−CNS hybrids with the schematic of the FEE measurement setup as the inset. The turn-on field (E_0) was evaluated by extrapolating two straight lines on both the lower and higher sides of the electric field in the F−N plot. Here, E_0 is measured to be 1.3 V/μm and a J_{FEE} value of 2.7 mA/cm^2 at E = 2.0 V/μm. It should be mentioned that we have tested five BNCD−CNS hybrids at three places of each sample in the same configuration at a constant cathode to anode distance. The FEE characteristics of these five BNCD−CNS hybrid-based cathodic devices were reproducible three times without altering their emission properties (J_{FEE}−E characteristics).

Generally, the FEE process from a material is modeled by the F−N model[1]

$$J_{FEE} = (A\beta^2E^2/\varphi)\exp(-B\varphi^{3/2}/\beta E)$$

where $A = 1.54 \times 10^{-6}$ A eV/V, $B = 6.83 \times 10^9$ eV$^{-3/2}$ V/m, β is the field-enhancement factor, and φ is the work function of the emitters. The inset image of Figure 3a displays the F−N plot, viz. ln (J_{FEE}/E^2) versus $1/E$, which fits well with a straight line, representing that the BNCD−CNS hybrids obey the F−N rule. The β value can be calculated from the slope of the fitted line using the following equation

$$\beta = -6.8 \times 10^3 \times \varphi^{1.5}/m$$

where m is the slope of the straight line in the high field regime.

Generally, the aspect ratio, screen effect, and tip geometry of the nanostructures determine the β-value. By keeping the φ value as 5 eV,[10,28] the calculated β for the BNCD−CNS hybrids is 6780. This value is greater than that of a CNT array (2916),[9] nitrogen-doped diamond nanorods (3320),[10] graphene nanoflakes (1560),[14] graphene/carbon nanofilament (4930),[20] and diamond-like carbon−CNTs (5227).[23] The FEE lifetime (τ_{FEE}-value) of the BNCD−CNS hybrids is a significant factor for field emission applications. To investigate the τ_{FEE}-value of these BNCD−CNS hybrids, their emission was monitored for different applied voltages, 1.85, 1.90, 1.95, and 1.98 V/μm above a period of 780 min, where the J_{FEE} value increases from 1.06, 1.50, 2.03 to 2.55 mA/cm^2, respectively, with the increase of the applied field (Figure 3b). In all cases, the fluctuations of J_{FEE} are below 5%, and the

DOI: 10.1021/acsami.9b17942
ACS Appl. Mater. Interfaces 2019, 11, 48612−48623

J_{FEE} values last for more than 780 min without showing signs of emission current decay, indicating excellent performance in emission stability for these hybrid materials. Interestingly, the FEE performance of the BNCD−CNS hybrids exhibits significant enhancements compared to other hybrid materials, as tabulated in Table S2.

Furthermore, the localized FEE properties of the BNCD−CNSs hybrids were also investigated by the AFM-based PF-TUNA technique[40] so as to directly locate the precise electron emission sites locally to understand the role of the BNCD and the CNSs materials on improving the FEE characteristics. Figure 4a shows the AFM surface morphology along with the

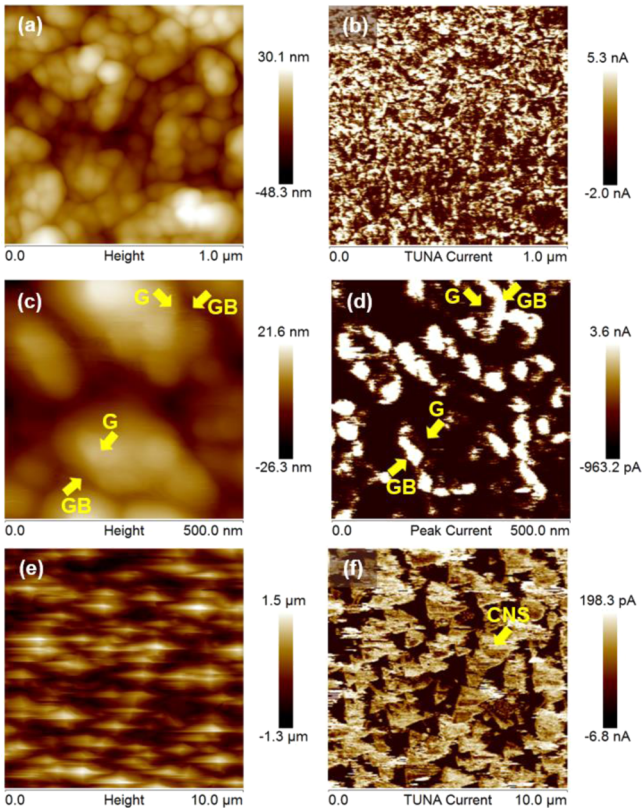

Figure 4. (a) AFM topography and (b) corresponding PF-TUNA image corresponding to the BNCD region of the BNCD−CNS hybrids acquired at −3 V. (c) High-resolution AFM and (d) corresponding PF-TUNA image corresponding to the BNCD region of the BNCD−CNS hybrids acquired at −3 V. (e) AFM image of BNCD−CNS hybrids and (f) corresponding PF-TUNA image acquired at −1 V.

representing PF-TUNA current mapping image (Figure 4b) of the BNCD films. The PF-TUNA current mapping was measured at an applied sample bias of −3.0 V. Figure 4a reveals that the BNCD films contain cauliflower-like aggregates of small diamond grains. The PF-TUNA image in Figure 4b reveals bright regions, which signify better electron emission. To locate exactly the field emission sites in the BNCD films, high-resolution AFM (HRAFM) micrograph was taken (Figure 4c) with the corresponding PF-TUNA current mapping in Figure 4d. The bright and dark regions in the PF-TUNA image (Figure 4d) resembles the GB and grains (G) of the HRAFM image, which evidently illustrates that the electrons are predominantly emitted from the GBs (bright regions) rather than the grains (dark regions). Hence, the more bright regions from the GBs prove that the existence of graphite at the GBs makes the electrons to transport very easily in the GBs. Moreover, a typical AFM micrograph of the whole BNCD−CNS hybrids is shown in Figure 4e,f, which represents the PF-TUNA current mapping taken at a sample bias of −1.0 V, corresponding to the AFM micrograph in Figure 4e. Again, the brighter regions in Figure 4f signify more emission current. Consequently, it is evident through Figure 4f that the emission sites are preferentially seen from the CNSs and the darker regions are from the BNCD films because it is known that CNSs are more conductive than BNCD films.

The question to be answered is what is the role of boron and nitrogen, whose presence in the BNCD−CNS hybrids were confirmed through Raman, XPS, and SIMS studies, on enhancing the FEE characteristics? First, in relation to boron doping, many debatable models have already been proposed for its behavior on enhancing the FEE properties. It is reported that the accumulation of holes because of boron doping increases the field enhancement,[41] besides the increase in the electrical conductivity of the BNCD films. A sub-band-based FEE model has also been proposed by other researchers.[42] Moreover, boron content in BNCD films is not reliable as compared to the doping in microcrystalline diamond films.[43] Hence, it is hard to draw a conclusion on the effect of boron for enhancing the FEE of BNCD−CNS hybrids. Second, the introduction of N_2 in diamond growth provides an amorphous phase. Upon annealing, the amorphous phase at the GB was converted to a graphitic phase, resulting in the increase in the conduction paths for the electrons in the material. Therefore, incorporation of N_2 contributes to a rise in the density of states at the Fermi level, resulting in enhanced FEE characteristics.[44] From the above observations, the superior FEE behavior of the BNCD−CNS hybrids could be credited to the origin of sharp edges at the CNSs and the induction of the graphitic phases at the GB of the BNCD films. The numerous vertically aligned sharp geometric protrusions of the nanospikes with a smaller curvature radius facing the anode, as shown in Figure 1a, which is commonly considered to have a fast electron transport rate, and the sharp edges at the CNSs can enhance the local FEE,[16,39] thus resulting in the low E_0 and high β values.

Microplasma Source. Microplasma sources are gas discharges in a small confined region that have recently received huge interest owing to their numerous valuable characteristics, such as high electron density, low power consumption, effectiveness with respect to cost, robustness, and portability in applications.[45] Principally, the devices based on microplasma sources create a novel area of research connecting plasma science, materials science, and optoelectronics.[46] Microplasma devices are promising for several applications including microdisplays, hazardous gas detectors, UV sources, plasma treatments, ozone production, silicon etching, and bioelectronics applications.[46−48] Different kinds of materials such as Mo, Al_2O_3, boron nitride, zinc oxide, CNTs, and silicon have been applied as cathodes in microplasma devices.[13,14,28,39,46] However, these materials as the cathodes in the microplasma devices show short lifetime and poor stability because the materials are exposed to severe plasma ion bombardment.[13,14,18,28,49] Moreover, a cathode material for microplasma devices should possess a high proficiency in producing secondary electrons for a longer duration through plasma ion bombardment. The simulation work from Venkatraman et al. also shows that a high FEE material can

DOI: 10.1021/acsami.9b17942
ACS Appl. Mater. Interfaces 2019, 11, 48612−48623

prominently improve the characteristics of a microplasma device.[50]

As BNCD−CNS hybrids possess superior FEE properties particularly in terms of high lifetime (cf. Figure 3b) and as diamond, particularly, has a high γ-coefficient, it is logical to apply BNCD−CNS hybrids as a microplasma device cathode. The plasma illumination (PI) characteristics of the BNCD−CNS hybrid-based cathode in a microplasma device carried out in a harsh Ar gas environment are shown in Figure 3c,d. The corresponding measurement setup for the microplasma device is shown in the inset of Figure 3c. The inset I of Figure 3d shows the PI images of the microplasma devices, which reveal that the plasma is triggered at a low voltage of 270 V and a systematic increase in the intensity of the plasma is observed while increasing the applied voltage. Figure 3c shows the plasma current density (J_{PI})−applied field (E) curve of the BNCD−CNS-based microplasma devices. It can be seen that plasma is ignited at a threshold field of E_{th} = 0.27 V/μm and the J_{PI} value reaches 16.2 mA/cm^2 at E = 0.50 V/μm (applied voltage = 550 V).

Furthermore, the plasma lifetime stability (τ_{PI}) of BNCD−CNS hybrids was evaluated by monitoring the J_{PI} value of 5.0 mA/cm^2 (corresponding to E = 0.32 V/μm) over a long period of time. Figure 3d establishes that for the BNCD−CNS hybrids as microplasma cathodic devices, the intensity of the plasma also remains stable after 545 min (inset II of Figure 3d), which indicates the high stability of these hybrids as compared to other diamond-based microplasma cathodic devices as reported (Table S3). Consequently, the benefit of the superior FEE properties as emitters, for the BNCD−CNS hybrids along with high hardness and a large γ-coefficient for the BNCD films, which reveals high robustness and high PI intensity for these materials, shows that the BNCD−CNS hybrids have significant potential for applications as a microplasma device cathode.

Now, the question yet to be answered is why do the BNCD−CNS hybrids, which possess a FEE turn-on field (E_0) markedly larger than the plasma threshold field (E_{th}), lead to enhanced PI performance? A potential description is as follows: before turning-on the Ar plasma, the BNCD−CNS hybrids employed as cathodes in the microplasma device required a threshold field (E_{th}) to initiate the ignition of plasma. E_{th} is low as compared to the FEE E_0 value of the BNCD−CNS hybrids, and the secondary electrons only contribute for ionizing the Ar gas molecules. Hence, the relatively larger E_0 of FEE is not helpful in contributing to the plasma current density (J_{PI}) of the microplasma devices. However, once the plasma is triggered, a few micron thick plasma sheath is generated near the cathode. The bulk of the plasma performed as an electron conduction path so that the voltage supplied to the anode will apply onto the plasma sheath. The electric field applied to the cathode will increase to around 0.32 V/μm (e.g., for an applied voltage of 320 V with 10 μm plasma sheath), which is noticeably higher than the FEE E_0 value (E_0 = 1.3 V/μm). The BNCD−CNS hybrids emit enormous numbers of electrons, and the plasma is ignited once the emitted electrons from the material attain the large kinetic energy of 15.7 eV adequate for ionizing the Ar gas molecules, and consecutively, there is an increase in the ionization of the Ar gas molecules along with a noticeable increase in the plasma density. Consequently, BNCD−CNS hybrids achieved a higher J_{PI}-value when employing them as cathodes in a microplasma device.

TEM Microstructure. To understand why the BNCD−CNS hybrids exhibit superior FEE and microplasma behaviors, the microstructure and the bonding structure of these hybrids were investigated by transmission electron microscopy (TEM) and electron energy loss spectroscopy (EELS). A low-magnification bright field TEM micrograph (BF-TEM) for the BNCD films is displayed in inset "a$_1$" of Figure 5a,

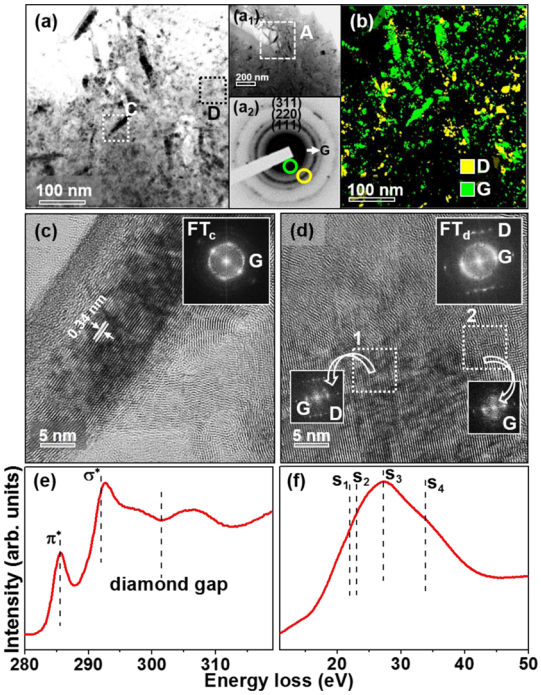

Figure 5. (a) High magnification BF-TEM micrograph corresponding to the BNCD region of the BNCD−CNS hybrids. Image (a) is taken from region "A" designated in the low magnification BF-TEM image, which is shown as inset (a$_1$), whereas the corresponding SAED pattern is shown as inset (a$_2$). (b) Composed DF TEM image corresponding to the TEM micrograph in (a) to mark the diamond and graphite regimes. (c) HRTEM micrograph, the structure image, taken at the region marked as "C" in (a) with the FT diffractogram corresponding to entire structure image is shown as the inset. (d) HRTEM micrograph, the structure image, taken at the region marked as "D" in (a) with the FT diffractogram corresponding to entire structure image shown as inset "FT$_d$", whereas the regions "1" and "2" show the FT images corresponding to diamond and graphite phases, respectively. (e) Core-loss and (f) plasmon-loss EELS spectra of the BNCD−CNS hybrids corresponding to BF-TEM micrograph in (a).

suggesting the formation of carbon nanoclusters of the acicular geometry evenly distributed among the amorphous carbon matrix. Figure 5a shows a high-magnified TEM micrograph of the marked area "A" from inset "a$_1$" in Figure 5a, which evidently shows the existence of acicular nanoclusters (dark contrast). The selective area electron diffraction (SAED) pattern (inset "a$_2$" of Figure 5a), corresponding to the high-magnified TEM micrograph, contains diffraction rings representing the (111), (220), and (311) diamond lattices, and the presence of sp^2-bonded carbon in this hybrid is indicated by a very bright diffuse ring at the center of the SAED pattern. Dark-field (DF) images are used to clearly elucidate the distribution of the phase constituents in the material, which were acquired from the diffraction segments of the SAED corresponding to the diamond and graphite phases (yellow and green rings; inset "a$_2$" of Figure 5a) and then

DOI: 10.1021/acsami.9b17942
ACS Appl. Mater. Interfaces 2019, 11, 48612−48623

superimposed to form a composed DF (c-DF) image. The c-DF image displayed in Figure 5b noticeably reveals the presence of acicular nanoclusters, which are of graphitic phases (green color), and the nanosized diamond grains (yellow color). These phases were distributed evenly among the matrix, which are amorphous carbon, in the BNCD region.

Figure 5c,d show the high-resolution TEM (HRTEM) micrographs of the BNCD films corresponding to the regions "C" and "D" in Figure 5a. The Fourier transformed (FT) diffractogram of the whole structure image in Figure 5c, FT_c, illustrates the diffraction spots organized in a ring representing the graphitic phase. Moreover, the 0.34 nm interlayer spaced parallel fringes in the inset of Figure 5c confirm that the acicular nanoclusters are only crystalline nanographite.[51] However, Figure 5d contains both nanosized diamond particulates and graphitic phases, which are identified from the FT_d image, corresponding to the whole structure image of Figure 5d, containing faint diffraction spots indicating diamond (designated as D) and a strong new-moon-like central diffused ring indicating graphite (designated as G), respectively. The FT images shown as the inset of Figure 5d, which correspond to the regions marked "1 and 2" in Figure 5d, indicate the diamond and graphitic phases, respectively.

The carbon K-edge EELS in TEM was used to study the different carbon phases in the BNCD films. The core-loss EELS spectrum of the BNCD films shown in Figure 5e indicates that the BNCD films contain both sp^3-bonded carbon (i.e., diamond), represented by a sharp peak at 291 eV (σ^*-band) and a dip in the vicinity of 302 eV,[52] and sp^2-bonded carbon specified by a π^*-band at 285 eV.[53] The plasmon-loss EELS measurements in TEM were further carried out to discriminate between graphite and amorphous carbon phases. Figure 5f shows the plasmon-loss EELS spectrum of the BNCD films, which reveals a peak around 27 eV (S_3) confirms the presence of graphite and a peak near 33 eV (S_4) along with a shoulder near 23 eV (S_2) (Figure 5f) indicate the presence of diamond in the BNCD films.[54] The peak at 22 eV (S_1) representing amorphous carbon phase is not evident in Figure 5f. Based on these TEM and EELS investigations in Figure 5, it is evident that the BNCD materials contain a mixture of nanosized diamond grains of equi-axed geometry and well-crystallized nanographitic clusters of the acicular geometry, along with a large proportion of randomly oriented spherical nanographitic clusters, distributed among the amorphous carbon matrix.

Figure 6 shows the TEM microstructure of CNSs. The BF-TEM micrograph of the CNSs displayed in Figure 6a discloses the existence of ball-like nanostructures of size around 50−200 nm as well as the needle-like CNSs that are about 100−200 nm in width. The SAED pattern shown as Figure 6c corresponding to the BF-TEM of Figure 6a brings out the presence of the (111), (220), and (311) diffraction rings, along with the existence of a strong central diffused ring, revealing that the CNSs are predominately the sp^2-bonded graphitic phase. Remarkably, a ring-shaped extra weak diffraction spots specified by an arrow in the inset of Figure 6c agrees to an allotrope of diamond called (200) *n-D* with a cell parameter of 0.356 nm and a space group of *Fm*3*m* symmetry.[52,55] The *n-D* clusters can be viewed as incompletely crystallized diamond clusters, that is, they formed earlier than the development of diamond nuclei. The magnified c-DF image in Figure 6b taken from region "B" of Figure 6a, which was acquired from different segments of SAED shown in Figure 6d, clearly shows

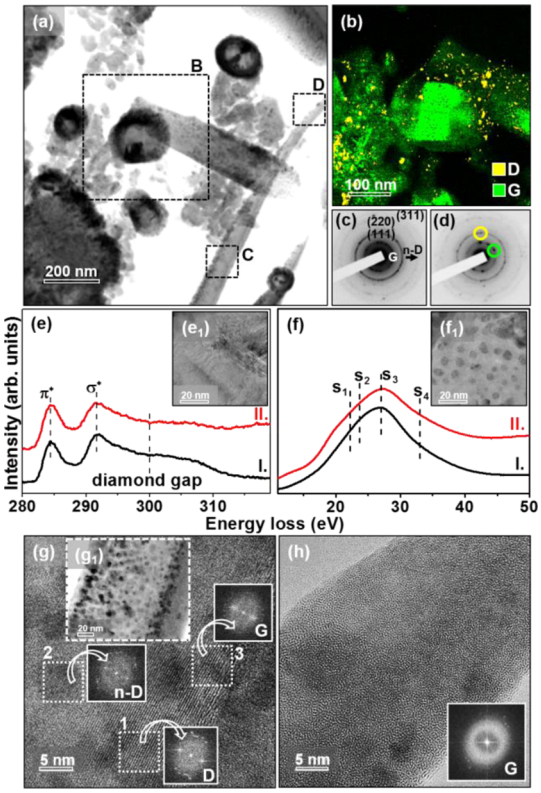

Figure 6. (a) BF-TEM micrograph corresponding to the spike region of the BNCD−CNS hybrids, whereas the corresponding SAED pattern is shown (c). (b) Composed DF TEM image corresponding to region "B" of (a). The DF images were acquired from different segments of SAED shown in (d) and then superimposed, where the D region (yellow color) is the diamond and G region (green color) is the graphitic phase. Spectra "I" in (e,f) represent the core-loss and plasmon-loss carbon K-edge EELS spectrum of spherical balls (region B in "G"), whereas spectrum II in (e,f) represent the core-loss and plasmon-loss carbon K-edge EELS spectrum taken from the structure image at the bottom region of the nanospikes ["D" region in (a)]. (g) HRTEM micrograph, the structure image, of the region shown as the bright field TEM micrograph in inset g_1, which was taken from region C of (a), representing the bottom region of the nanospike. The regions "1", "2" and "3" show the FT images corresponding to diamond, *n-diamond* (*n-D*) and graphite phases, respectively. (h) The structure image taken from region D of (a), which represents that the top region of the nanospikes are only graphitic in nature. This is understood from the FT image [inset of (h)] that corresponds to the whole structure image in (h).

that the spherical balls are of graphitic phases (green color) and the nanosized diamond particulates (yellow color) are evenly distributed surrounding the spherical graphitic balls. The carbon K-edge core-loss EELS spectrum I taken from the structure image of spherical balls (inset I of Figure 6e) indicates the π^* band at 285.0 eV, representing these spherical balls comprised only graphitic phases and no diamond phase. The plasmon-loss EELS spectrum I in Figure 6f confirms the findings from the core-loss EELS spectrum I in Figure 6f.

The high-magnified TEM micrograph shown in inset g_1 of Figure 6g, which was taken from region C of Figure 6a, indicates that the bottom region of the nanospikes contains nanosized clusters around 5−10 nm in size. The structure image displayed in Figure 6g clearly specifies that this bottom region contains different phases; nanosized diamond (FT_1), *n-D* (FT_2), and graphite (FT_3) phases. The core-loss (spectrum

DOI: 10.1021/acsami.9b17942
ACS Appl. Mater. Interfaces 2019, 11, 48612−48623

II of Figure 6e) and plasmon-loss spectra (spectrum II of Figure 6f) (cf. HRTEM micrograph of Figure 6g) further confirm that this bottom region is predominated with graphitic nanoclusters. It is to be noted that the signature of diamond peaks from core-loss EELS (spectrum II, Figure 6e) is absent, demonstrating that the diamond lattices contain more defects such as *n-D* particulates. In contrast, the top region of the nanospikes are only graphitic in nature, which is understood from the structure image in Figure 6h taken from region D of Figure 6a and the FT image (inset of Figure 6h) that relates to the whole HRTEM micrograph in Figure 6h. Consequently, combining the description of the microstructure of BNCD−CNS hybrids implies that these materials are actually nanocarbon hybrid materials, which are predominantly with well-crystallized graphitic clusters dispersed with the nanosized diamond particulates.

Formation Mechanism. It should be noted that the TEM microstructures and the EELS spectra shown in Figures 5 and 6 clearly indicate that the nanodiamond clusters contained in the materials gradually disappeared while the CNSs grew. This implies that CNSs probably stemmed from the acicular nanographite clusters enclosed in the BNCD layer, which are predominantly the graphite phase. In order to examine the growth mechanism of the BNCD−CNS hybrids, together with the identification of carbon allotropes in the BNCD−CNS hybrids, the optical emission spectroscopy (OES) spectra of microwave plasma during the biased carburization (phase I) and growth (phase II) stages were recorded. Figure 7 shows

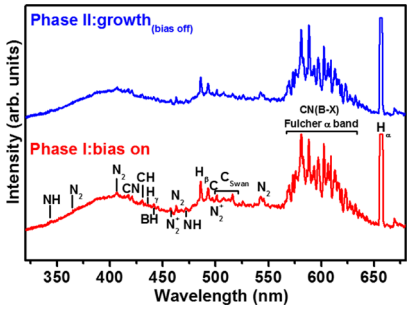

Figure 7. OES spectra of the $H_2/CH_4/B_2H_6/N_2$ microwave plasma during biased carburization (phase I) and growth (phase II) i. The emission spectra recorded during these two different CVD phases do not show substantial variances. The growth process of BNCD−CNS in the presence of nitrogen involves H, CH_x, and CN radicals. The presence of an N_2 band at 358 nm and a CN band at 418 nm confirms the contribution of nitrogen-based species in the plasma. These nitrogen species modify the plasma reactions by changing the concentrations of other growth species such as C_2 and CH (C_2 Swan bands at 516.5 nm; CH line at 431.4 nm) and play a key role in the formation of diamond and graphitic phases. The plasma chemistry of the boron precursor, that is, diborane (B_2H_6), is evidenced by the BH band at 433 nm, the most representative fingerprint of boron in the plasma.

that the emission spectra of the plasma recorded during two different phases of the CVD process do not show substantial differences. This observation implies that the difference in the formation process of BNCD and CNS is mainly driven by the reactions of the growth plasma and surface induced by the biased voltage. The important species contained in the OES spectra are listed in Table S4. The growth process of BNCD−CNS hybrids involves H, a CH_x band at 431.4 nm, a N_2 band at 358 nm, a CN band at 418 nm, and C_2 Swan bands at 516.5 nm,[56] which show a major part in the origin of the diamond and graphitic phases. The ratios of intensity of the C_2 band at 516.5 nm associated to the H_β lines (C_2/H_β) reach values up to 0.66 and 0.78 for the biased enhanced carburization (spectrum I) and standard CVD growth phases (spectrum II), respectively. The C_2 species are the cause for the formation of single carbon species that shape the structure or nucleate the spikes. Furthermore, the CH relative to the H_β line (CH/H_β) reveals a decrease in the value from 1.56 to 1.47 for biased enhanced carburization (phase I) and standard CVD growth (phases II) stages. The surface of the diamond seeds and clusters are attached by the CN and HCN species, which enriches the diamond growth, whereas the presence of CH species tends to passivate the as-formed diamond nuclei, preventing the diamond nuclei to grow further as a large-sized diamond grain, which explains why the diamond particles in BNCD films remained very small in size. Furthermore, the BH band at 433 nm showed in Figure 7 represents the fingerprint of boron in the growth plasma, confirming that the BNCD bottom layer and CNSs are doped with boron. The BH emission is slightly larger during phase-biased enhanced carburization (phase I) than standard CVD growth phases (phase II).

Nevertheless, the change in abundance of the C_2, N_2, H_x, CH_x, CN, and BH radicals attributable to the bias applied in phase I (bias-enhanced carburization) is not significant and seems not to be the main feature resulting in the change of the growth mechanism to form the BNCD and CNSs. On the other hand, the kinetic energy of the charged carbonaceous species increases noticeably because of the application of bias. It has been observed recently that the increase in kinetic energy of the adsorbed species, no matter whether it results from the increase in substrate temperature or the application of bias voltage, facilitates the crystallization of the adsorbed adatoms.[57] Among the important species that exist in the $CH_4/H_2/B_2H_6/N_2$ plasma, the C_2 and CH species grow carbonaceous materials (diamond, graphite, and amorphous carbons), whereas CN_x and H_x and so forth are the species which modify the microstructure of the phases. The formation of crystalline clusters is difficult in the presence of complicated species in the $CH_4/H_2/B_2H_6/N_2$ plasma, especially in the presence of CH_x and CN_x species. Therefore, the phase II (growth phase) tends to grow amorphous carbons or related materials. Only when the bias is applied, can the adsorbed C_2 species form crystalline clusters. In the bias enhanced carburization phase (phase I), the nanographitic clusters will form preferentially, as they were energetically favorable, as compared with the formation of nanodiamond clusters.[49,57,58] Moreover, the nanographitic clusters are of acicular geometry, which is also attributable to the application of this bias. This process explains excellently the growth of the BNCD layer in phase I. When no bias is applied in the growth period (phase II), the matrix of amorphous carbon ceases to grow. Only the acicular nanographitc clusters serve as the nuclei for the growth of nanospikes.

The abovementioned processes for the formation of the BNCD bottom layer and subsequently the outgrowth of the spike-like carbon nanostructures is schematically illustrated in Figure 8. That is, because of the application of bias, the carbon clusters start to form nanosized crystalline clusters (sp^2- or sp^3-bonded carbons) and amorphous carbon as a matrix (Figure 8b). Notably, the preseeding procedure (Figure 8a) is necessary to induce the nucleation of nanosized crystalline

DOI: 10.1021/acsami.9b17942
ACS Appl. Mater. Interfaces 2019, 11, 48612−48623

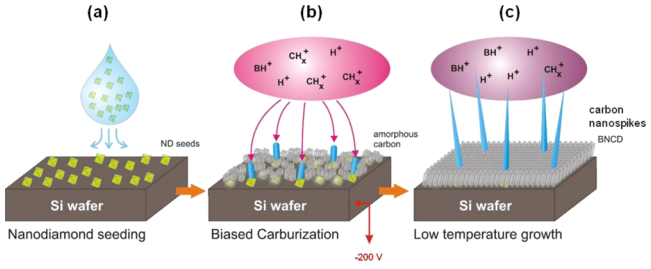

Figure 8. Scheme of the growth mechanism of BNCD−CNS hybrids in the $H_2/CH_4/B_2H_6/N_2$ microwave plasma—(a) nanodiamond seeding on the Si wafer prior to diamond growth and (b,c) subsequential steps of nanospike formation of BNCD−CNS hybrids in the microwave plasma.

clusters. During the phase I process, some nanographitic clusters of acicular geometry were induced. The nanodiamond particulates of the equi-axed geometry were also formed occasionally, evenly distributed among the amorphous carbon matrix that resulted in BNCD layers. In phase II of the MPECVD process, the bias voltage was removed. The growth of the BNCD layer ceased owing to the insufficient kinetic energy of the species. Only the nanographitic clusters continued to grow because of the smaller surface energy for the formation of graphite materials and the existence of nanographitic nanoneedles, which serve as nanospike nuclei. The scheme shown in Figure 8 is in agreement with other previous findings[58,59] and supported by the SEM, Raman, XPS, and TEM studies reported in this paper.

CONCLUSIONS

This work presents a one-step fabrication of hybrid carbon materials based on CNS together with a BNCD layer. This hybrid structure overwhelms numerous problems that of in the CNT tips, especially in a plasma environment. The synthesized BNCD−CNS hybrids showed superior FEE properties with a low E_0 of 1.3 V/μm, a large β-factor of 6780, a high J_{FEE} of 2.7 mA/cm, and a long-lasting electron emission stability of 780 min at different applied fields. The excellent FEE properties of these hybrids are derived mainly from the synergistic effects between CNS and BNCD, which possess a large aspect ratio and numerous emission sites. Such hybrids not only exhibit excellent FEE properties but also display high robustness in a plasma environment when they are employed as a cathode in a microplasma device. Overall, this study proposes that the presented BNCD−CNS hybrids appear as a prospective electron source for flat panel displays and plasma displays.

EXPERIMENTAL METHODS

Catalyst Free, One-Step Growth of BNCD−CNS. A MPECVD (2.45 GHz Seki Technotron AX5400S, Japan) system was used to synthesize the BNCD−CNS hybrids on silicon substrates. Prior to the CVD growth, Si substrates were nucleated in diamond slurry (BlueSeeds, AdamasNano, USA) by using the ultrasonication process. It is reported that a high seeding density of 10^{10} cm^{-2} was achieved using this seeding procedure.[60] Studied surfaces have been grown utilizing the following growth parameters: gas mixture—$H_2/CH_4/B_2H_6/N_2$ (85:5:9:1%) of total flow rate 265 sccm; [B]/[C] ratio of (0.0167%) 16 700 ppm; microwave power set to 1100 W; process pressure of 35 Torr; and a growth time equal to 20 h. An induction heater was employed to heat the substrate holder to 650 °C, and a thermocouple was used to measure the substrate temperature. To enhance the seeding and nucleation process of the BNCD−CNS surfaces, a negative bias voltage of −200 V was applied to the stage during the first 20 min of CVD growth.

Material Characterization. The surface morphology, the microstructure, and the bonding structure of these hybrid materials were examined with a scanning electron microscope [FEI Quanta FEG 250 using a 10 kV beam accelerating voltage with an secondary electron Everhart−Thornley detector working in the high-vacuum mode (pressure 10^{-4} Pa)], transmission electron microscopy (Jeol 2100F), and an EELS (Gatan Enfina) in TEM, respectively. The Raman spectra of the materials were recorded using a micro Raman spectrometer (InVia, Renishaw, UK) equipped with a 514 nm argon-ion laser as an excitation source in combination with a 50× objective (NA = 0.5) and a 10 μm confocal aperture. Spectra were recorded in a range of 100−3200 cm^{-1}. High-resolution XPS studies were carried out on an ESCALAB 250 Xi from Thermofisher Scientific. The spectroscope is equipped with the Al Kα source. The pass energy was 20 eV and the spot size diameter was 650 μm. Charge compensation was controlled through the low-energy electron and low-energy Ar^+ ions emission by means of a flood gun (emission current 150 μA, beam voltage 2.1 V, filament current 3.5 A). Avantage software (Thermofisher Scientific) was used for deconvolution purposes. Elemental depth profiling analysis of the C, B, BN, CN, and N in BNCD−CNS samples was carried out by time-of-flight SIMS (TOF-SIMS5, ION-TOF GmbH) using the Bismuth (Bi^+) ion. 2D images of the depth profiling were generated for the quantitative elemental analysis. The plasma constituents were analyzed by OES using a 0.3 m monochromator (SR303i, Andor) equipped with 1200 grooves per mm grating and an ICCD detector (DH740, Andor).

FEE Measurements. To evaluate the FEE performance of the BNCD−CNS hybrids, a hybrid was installed in a high vacuum chamber of pressure below 10^{-6} Torr. A custom-made tunable parallel plate capacitor, with a molybdenum tip of 2 mm diameter, was used as the anode at a fixed distance of 200 μm from the cathode (emitting sample). The separation of the anode from the sample was measured using a digital micrometer. The setup was completed by electrically connecting the electrodes to a computer-controlled Keithley K2410 source/measure unit to acquire the current densities versus electrical field (J_e−E) characteristics, and the data were analyzed using the F−N theory.

PF-TUNA Measurements. Multimode VIII AFM with a Nanoscope V controller and PF-TUNA module (Bruker, CA, USA) was used to perform the PF-TUNA measurements at ambient conditions. The measurement details have been elucidated elsewhere.[60] In brief, to create an electrical contact between the BNCD−CNS hybrids and the AFM tip, conductive silver paint (G3790 Agar Scientific) was used to attach the base of the Si substrate to a metallic disc. PeakForce feedback helped collect the topographic and tunneling current information. A Pt−Ir coating on the tip of the cantilever, with a spring constant of 9.8 N/m, allowed the measurement of current from the sample surface when a bias was applied between the tip and the sample. Images were recorded at a resolution of 512 × 512 pixels with a tip bias of a few volts with a lower scan rate of 0.1 or 0.2 Hz to allow the maximum time for the TUNA current measurement in a particular position. A number of tests were performed to confirm that the measured TUNA current is a true reflection of the emission current of the BNCD−CNS surface and not from any artifacts present on the surface. The recorded emission currents, with tip−sample biases varying from the mV to V range, were in the range of few pA to a few nA per emission site.

PI Measurements. The PI characteristics of the BNCD−CNS hybrids were evaluated using a microplasma device with a parallel plate configuration, in which the indium-tin oxide (ITO)-coated glass plates (the anode) were separated from the cathode (BNCD−CNS hybrids) by a 1.0 mm thick Teflon spacer. A 3.0 mm in diameter circular hole was cut out of the Teflon spacer to create a cylindrical cavity. The devices were kept in a vacuum chamber with a base pressure of 0.01 mTorr and externally connected to a dc power supply through a 500 kΩ resistor. The reliability of the measurements was improved by heating the samples at 200 °C for 1 h to remove any moisture on the surface of the samples. Argon at the rate of 10 sccm

DOI: 10.1021/acsami.9b17942
ACS Appl. Mater. Interfaces 2019, 11, 48612−48623

was flowed throughout the measurements and a plasma was excited in between the ITO and BNCD−CNS hybrids by supplying a dc voltage from 0 V to breakdown and was then increased linearly up to the maximum voltage of 500 V (at room temperature). The plasma current density (J_{PI}) versus applied field (E) was acquired at a constant pressure of 100 Torr using a Keithley 2410 current source electrometer. The plasma was observed through the ITO using a USB microscope, and snapshots were recorded for different applied voltages to characterize the PI behavior of the microplasma devices.

■ ASSOCIATED CONTENT

Supporting Information

The Supporting Information is available free of charge at https://pubs.acs.org/doi/10.1021/acsami.9b17942.

2D mapping of SIMS depth profiles of the growth species such as C_2, BH, CH, CN, and B in the $H_2/CH_4/B_2H_6/N_2$ plasma. The C_2 species possess high intensity with high bright regions. The BH and CH species are almost at the same intensity followed by the CN, O, and B species. High-resolution XPS analysis of different C 1s, B 1s, and N 1s chemical states in the BNCD−CNS hybrids, deconvoluted using the above-described model. FEE properties of BNCD−CNS hybrids compared to other hybrid nanostructures reported in the literature. PI properties of BNCD−CNS hybrids compared to other diamond-based microplasma cathodic devices reported in the literature. The designation of the species derived from the OES spectra of the $CH_4/H_2/B_2H_6/N_2$ plasma used for growing the BNCD and CNSs (PDF)

■ AUTHOR INFORMATION

Corresponding Authors

*E-mail: sankaran.kamatchi@uhasselt.be (K.J.S.).
*E-mail: ken.haenen@uhasselt.be (K.H.).

ORCID

Kamatchi Jothiramalingam Sankaran: 0000-0002-4468-0541
Jeong Young Park: 0000-0002-8132-3076
I-Nan Lin: 0000-0001-6474-2394
Ken Haenen: 0000-0001-6711-7367

Author Contributions

K.J.S. and M.F. have contributed equally to this work. The manuscript was written through contributions of all authors. All authors have given approval to the final version of the manuscript.

Notes

The authors declare no competing financial interest.

■ ACKNOWLEDGMENTS

This work is supported by the Flemish Methusalem "NANO" network, the Polish National Science Center (NCN) under Grant No. 2016/21/B/ST7/01430, 2015/17/D/ST5/02571, the National Center for Science and Development Grant Techmatstrateg No. 347324 and Foundation for Polish Science grant number POIR.04.04.00-00-1644/18 and the Institute for Basic Science [IBS-R004]. The DS funds of the Faculty of Electronics, Telecommunications and Informatics of the Gdansk University of Technology are also acknowledged.

■ REFERENCES

(1) Fowler, R. H.; Nordheim, L. Electron Emission in Intense Electric Fields. *Proc. R. Soc. London, Ser. A* **1928**, *119*, 173−181.

(2) Xavier, S.; Mátéfi-Tempfli, S.; Ferain, E.; Purcell, S.; Enouz-Védrenne, S.; Gangloff, L.; Minoux, E.; Hudanski, L.; Vincent, P.; Schnell, J.-P.; Pribat, D.; Piraux, L.; Legagneux, P. Stable Field Emission from Arrays of Vertically Aligned Free-standing Metallic Nanowires. *Nanotechnology* **2008**, *19*, 215601.

(3) Collins, C. M.; Parmee, R. J.; Milne, W. I.; Cole, M. T. High Performance Field Emitters. *Adv. Sci.* **2016**, *3*, 1500318.

(4) Zhang, Q. Y.; Xu, J. Q.; Zhao, Y. M.; Ji, X. H.; Lau, S. P. Fabrication of Large-Scale Single-Crystalline PrB6 Nanorods and Their Temperature-Dependent Electron Field Emission. *Adv. Funct. Mater.* **2009**, *19*, 742−747.

(5) Viskadouros, G.; Zak, A.; Stylianakis, M.; Kymakis, E.; Tenne, R.; Stratakis, E. Enhanced Field Emission of WS_2 Nanotubes. *Small* **2014**, *10*, 2398−2403.

(6) Pradhan, D.; Kumar, M.; Ando, Y.; Leung, K. T. Efficient Field Emission from Vertically Grown Planar ZnO Nanowalls on an ITO-Glass Substrate. *Nanotechnology* **2008**, *19*, 035603.

(7) Chen, L.; Yu, H.; Zhong, J.; Wu, J.; Su, W. Graphene based Hybrid/Composite for Electron Field Emission: A Review. *J. Alloys Compd.* **2018**, *749*, 60−84.

(8) Xu, J.; Chang, Y.; Gan, L.; Ma, Y.; Zhai, T. Ultrathin Single-Crystalline Boron Nanosheets for Enhanced Electro-Optical Performances. *Adv. Sci.* **2015**, *2*, 1500023.

(9) Zhang, Q.; Wang, X.-j.; Meng, P.; Yue, H.-x.; Zheng, R.-t.; Wu, X.-l.; Cheng, G.-a. High Current Density and Low Emission Field of Carbon Nanotube Array Microbundle. *Appl. Phys. Lett.* **2018**, *112*, 013101.

(10) Deshmukh, S.; Sankaran, K. J.; Srinivasu, K.; Korneychuk, S.; Banerjee, D.; Barman, A.; Bhattacharya, G.; Phase, D. M.; Gupta, M.; Verbeeck, J.; Leou, K. C.; Lin, I. N.; Haenen, K.; Roy, S. S. Local Probing of the Enhanced Field Electron Emission of Vertically Aligned Nitrogen-doped Diamond Nanorods and Their Plasma Illumination Properties. *Diamond Relat. Mater.* **2018**, *83*, 118−125.

(11) Zhou, S.; Chen, K.; Cole, M. T.; Li, Z.; Chen, J.; Li, C.; Dai, Q. Ultrafast Field Emission Electron Sources Based on Nanomaterials. *Adv. Mater.* **2019**, *31*, 1805845.

(12) Giubileo, F.; Di Bartolomeo, A.; Iemmo, L.; Luongo, G.; Urban, F. Field Emission from Carbon Nanostructures. *Appl. Sci.* **2018**, *8*, 526.

(13) Sankaran, K. J.; Srinivasu, K.; Leou, K. C.; Tai, N. H.; Lin, I. N. High Stability Electron Field Emitters Made of Nanocrystalline Diamond Coated Carbon Nanotubes. *Appl. Phys. Lett.* **2013**, *103*, 251601.

(14) Chang, T.; Lu, F.; Kunuku, S.; Leou, K.; Tai, N.; Lin, I. Enhanced Electron Field Emission Properties from Hybrid Nanostructures of Graphene/Si Tip Array. *RSC Adv.* **2015**, *5*, 2928−2933.

(15) Varshney, D.; Rao, C. V.; Mendoza, F.; Perez, K.; Guinel, M. J.-F.; Ishikawa, Y.; Weiner, B. R.; Morell, G. Electron Emission of Graphene-Diamond Hybrid Films Using Paraffin Wax as Diamond Seeding Source. *World J. Nano Sci. Eng.* **2012**, *02*, 126−133.

(16) Chang, I.-L.; Tsai, P.-H.; Tsai, H.-Y. Field Emission Characteristics of CNFB-CNT Hybrid Material Grown by One-step MPCVD. *Diamond Relat. Mater.* **2016**, *69*, 229−236.

(17) Tsai, P.-H.; Tsai, H.-Y. Fabrication and Field Emission Characteristic of Microcrystalline Diamond/Carbon Nanotube Double Layered Pyramid Arrays. *Thin Solid Films* **2015**, *584*, 330−335.

(18) Chang, T.-H.; Hsieh, P.-Y.; Kunuku, S.; Lou, S.-C.; Manoharan, D.; Leou, K.-C.; Lin, I.-N.; Tai, N.-H. High Stability Electron Field Emitters Synthesized via The Combination of Carbon Nanotubes and N2-Plasma Grown Ultrananocrystalline Diamond Films. *ACS Appl. Mater. Interfaces* **2015**, *7*, 27526−27538.

(19) Yuge, R.; Miyawaki, J.; Ichihashi, T.; Kuroshima, S.; Yoshitake, T.; Ohkawa, T.; Aoki, Y.; Iijima, S.; Yudasaka, M. Highly Efficient Field Emission from Carbon Nanotube-Nanohorn Hybrids Prepared by Chemical Vapor Deposition. *ACS Nano* **2010**, *4*, 7337−7343.

(20) Dai, W.; Chung, C.-Y.; Alam, F. E.; Hung, T.-T.; Sun, H.; Wei, Q.; Lin, C.-T.; Chen, S.-K.; Chin, T.-S. Superior Field Emission Performance of Graphene/Carbon Nanofilament Hybrids Synthe-

DOI: 10.1021/acsami.9b17942
ACS Appl. Mater. Interfaces 2019, 11, 48612−48623

sized by Electrochemical Self-exfoliation. *Mater. Lett.* **2017**, *205*, 223−225.
(21) Xiao, X.; Auciello, O.; Cui, H.; Lowndes, D. H.; Merkulov, V. L.; Carlisle, J. Synthesis and Field Emission Properties of Hybrid Structures of Ultrananocrystalline Diamond and Vertically Aligned Carbon Nanofibers. *Diamond Relat. Mater.* **2006**, *15*, 244−247.
(22) Zou, Y.; May, P. W.; Vieira, S. M. C.; Fox, N. A. Field Emission from Diamond-Coated Multiwalled Carbon Nanotue "teepee" Structures. *J. Appl. Phys.* **2012**, *112*, 044903.
(23) Zanin, H.; May, P. W.; Hamanaka, M. H. M. O.; Corat, E. J. Field Emission from Hybrid Diamond-like Carbon and Carbon Nanotube Composite Structures. *ACS Appl. Mater. Interfaces* **2013**, *5*, 12238−12243.
(24) Uppireddi, K.; Weiner, B. R.; Morell, G. Field Emission Stability and Properties of Simultaneously Grown Microcrystalline Diamond and Carbon Nanostructure Films. *J. Vac. Sci. Technol.* **2010**, *28*, 1202−1205.
(25) Koh, A. T. T.; Chen, T.; Pan, L.; Sun, Z.; Chua, D. H. C. Effective Hybrid Graphene/Carbon Nanotubes Field Emitters by Electrophoretic Deposition. *J. Appl. Phys.* **2013**, *113*, 174909.
(26) Liu, J.; Zeng, B.; Wang, X.; Wang, W.; Shi, H. One-step Growth of Vertical Graphene Sheets on Carbon Nanotubes and Their Field Emission Properties. *Appl. Phys. Lett.* **2013**, *103*, 053105.
(27) Nguyen, D. D.; Lai, Y.-T.; Tai, N.-H. Enhanced Field Emission Properties of a Reduced Graphene oxide/Carbon Nanotube Hybrid Film. *Diamond Relat. Mater.* **2014**, *47*, 1−6.
(28) Sankaran, K. J.; Yeh, C.-J.; Drijkoningen, S.; Pobedinskas, P.; Van Bael, M. K.; Leou, K.-C.; Lin, I.-N.; Haenen, K. Enhancement of Plasma Illumination Characteristics of Few-layer Graphene Diamond Nanorods Hybrid. *Nanotechnology* **2017**, *28*, 065701.
(29) Piazza, F.; Golanski, A.; Schulze, S.; Relihan, G. Trans-polyacetylene Chains in Hydrogenated Amorphous Carbon Films Free of Nanocrystaline Diamond. *Appl. Phys. Lett.* **2003**, *82*, 358−360.
(30) Nemanich, R. J.; Solin, S. A. First- and Second-order Raman Scattering from Finite-size Crystals of Graphite. *Phys. Rev. B* **1979**, *20*, 392−401.
(31) Bokobza, L.; Zhang, J. Raman Spectroscopic Characterization of Multiwall Carbon Nanotubes and of Composites. *eXPRESS Polym. Lett.* **2012**, *6*, 601−608.
(32) Sobaszek, M.; Siuzdak, K.; Ryl, J.; Sawczak, M.; Gupta, S.; Carrizosa, S. B.; Ficek, M.; Dec, B.; Darowicki, K.; Bogdanowicz, R. Diamond Phase (sp^3-C) Rich Boron-Doped Carbon Nanowalls (sp^2-C): Physicochemical and Electrochemical Properties. *J. Phys. Chem. C* **2017**, *121*, 20821−20833.
(33) Kolel-Veetil, M. K.; Gamache, R. M.; Bernstein, N.; Goswami, R.; Qadri, S. B.; Fears, K. P.; Miller, J. B.; Glaser, E. R.; Keller, T. M. Substitution of Silicon Within the Rhombohedral Boron Carbide (B_4C) Crystal Lattice Through High-Energy Ball Milling. *J. Mater. Chem. C* **2015**, *3*, 11705−11716.
(34) Wang, K.; Kang, X.; Kang, Q.; Zhong, Y.; Hu, C.; Wang, P. Improved Reversible Dehydrogenation of 2LIBH4-MgH2 Composite by the Controlled Formation of Transition Metal Boride. *J. Mater. Chem. A* **2014**, *2*, 2146−2151.
(35) Cermignani, W.; Paulson, T. E.; Onneby, C.; Pantano, C. G. Syntheis and Characterization of Boron-doped Carbons. *Carbon* **1995**, *33*, 367−374.
(36) Siuzdak, K.; Ficek, M.; Sobaszek, M.; Ryl, J.; Gnyba, M.; Niedziałkowski, P.; Malinowska, N.; Karczewski, J.; Bogdanowicz, R. Boron-Enhanced Growth of Micron-Scale Carbon-Based Nanowalls: A Route Toward High Rates of Electrochemical Biosensing. *ACS Appl. Mater. Interfaces* **2017**, *9*, 12982−12992.
(37) Chaudhari, N. K.; Song, M. Y.; Yu, J.-S. Heteroatom-doped Highly Porous Carbon from Human Urine. *Sci. Rep.* **2014**, *4*, 5221.
(38) Yang, J.; Xu, M.; Wang, J.; Jin, S.; Tan, B. A Facile Approach to Prepare Multiple Heteroatom-Doped Carbon Materials from Imine-Linked Porous Organic Polymers. *Sci. Rep.* **2018**, *8*, 4200.
(39) Sankaran, K. J.; Ficek, M.; Kunuku, S.; Panda, K.; Yeh, C.-J.; Park, J. Y.; Sawczak, M.; Michałowski, P. P.; Leou, K.-C.; Bogdanowicz, R.; Lin, I.-N.; Haenen, K. Self-organized Multi-layered Graphene-Boron Doped Diamond Hybrid Nanowalls for High-Performance Electron Emission Devices. *Nanoscale* **2018**, *10*, 1345−1355.
(40) Chubenko, O.; Baturin, S. S.; Baryshev, S. V. Scanning Probe Microscopy and Field Emission Schemes for Studying Electron Emission from Polycrystalline Diamond. *Appl. Phys. Lett.* **2016**, *109*, 113102.
(41) Wisitsora-at, A.; Kang, W. P.; Davidson, J. L.; Li, Q.; Xu, J. F.; Kerns, D. V. Efficient Electron Emitter Utlizing Boron-doped Diamond Tips with sp^2 Content. *Appl. Surf. Sci.* **1999**, *146*, 280−286.
(42) Kwon, S. J.; Shin, Y. H.; Asalm, D. M.; Lee, J. D. Field Emission Properties of the Polycrystalline Diamond Film Prepared by Microwave-Assisted Plasma Chemical Vapor Deposition. *J. Vac. Sci. Technol., B: Microelectron. Nanometer Struct.–Process., Meas., Phenom.* **1998**, *16*, 712−715.
(43) Lee, Y.-C.; Lin, S.-J.; Lin, I.-N.; Cheng, H.-F. Effect of Boron Doping on the Electron-Field-Emission Properties of Nanodiamond Films. *J. Appl. Phys.* **2005**, *97*, 054310.
(44) Panda, K.; Hyeok, J. J.; Park, J. Y.; Sankaran, K. J.; Balakrishnan, S.; Lin, I.-N. Nanoscale Investigation of Enhanced Electron Field Emission for Silver Ion Implanted/Post-annealed Ultrananocrystalline Diamond Films. *Sci. Rep.* **2017**, *7*, 16325.
(45) Mariotti, D.; Ostrikov, K. Tailoring Microplasma Nano-fabrication: From Nanostructures to Nanoarchitectures. *J. Phys. D: Appl. Phys.* **2009**, *42*, 092002.
(46) Schoenbach, K. H.; Becker, K. 20 years of Microplasma Research: A Status Report. *Eur. Phys. J. D* **2016**, *70*, 29.
(47) Ostrikov, K. Control of Energy and Matter at Nanoscales: Challenges and Opportunities for Plasma Nanoscience in a Sustainability Age. *J. Phys. D: Appl. Phys.* **2011**, *44*, 174003.
(48) Barekzi, N.; Laroussi, M. Effect of Low Temperature Plasmas on Cancer Cells. *Plasma Processes Polym.* **2013**, *10*, 1039−1050.
(49) Saravanan, A.; Huang, B.-R.; Manoharan, D.; Lin, I.-N. High-Performance Electron Field Emitters and Microplasma Cathodes Based on Conductive Hybrid Granular Structured Diamond Materials. *ACS Appl. Mater. Interfaces* **2017**, *9*, 4916−4925.
(50) Venkattraman, V.; Garg, A.; Peroulis, D.; Alexeenko, A. A. Direct Measurements and Numerical Simulations of Gas Charging in Microelectromechanical System Capacitive Switches. *Appl. Phys. Lett.* **2012**, *100*, 083503.
(51) Kalita, G.; Wakita, K.; Umeno, M. Low Temperature Growth of Graphene Film by Microwave Assisted Surface Wave Plasma CVD for Transparent Electrode Application. *RSC Adv.* **2012**, *2*, 2815−2820.
(52) Kovarik, P.; Bourdon, E. B. D.; Prince, R. H. Electron-Energy-Loss Characterization of Laser-Deposited a-C, a-C:H, and Diamond Films. *Phys. Rev. B: Condens. Matter Mater. Phys.* **1993**, *48*, 12123.
(53) Prawer, S.; Peng, J. L.; Orwa, J. O.; McCallum, J. C.; Jamieson, D. N.; Bursill, L. A. Size Dependence of Structural Stability in Nanocrystalline Diamond. *Phys. Rev. B: Condens. Matter Mater. Phys.* **2000**, *62*, R16360.
(54) Kurian, J.; Sankaran, K. J.; Thomas, J. P.; Tai, N. H.; Chen, H.-C.; Lin, I.-N. The Role of Nanographitic Phase on Enhancing the Electron Field Emission Properties of Hybrid Granular Structured Diamond Films: The Electron Energy Loss Spectroscopic Studies. *J. Phys. D: Appl. Phys.* **2014**, *47*, 415303.
(55) Hirai, H.; Kondo, K.-I. Modified Phases of Diamond Formed Under Shock Compression and Rapid Quenching. *Science* **1991**, *253*, 772−774.
(56) Sankaran, K. J.; Kumar, N.; Kurian, J.; Ramadoss, R.; Chen, H.-C.; Dash, S.; Tyagi, A. K.; Lee, C.-Y.; Tai, N.-H.; Lin, I.-N. Improvement in Tribological Properties by Modification of Grain Boundary and Microstructure of Ultrananocrystalline Diamond Films. *ACS Appl. Mater. Interfaces* **2013**, *5*, 3614−3624.
(57) Sankaran, K. J.; Huang, B.-R.; Saravanan, A.; Manoharan, D.; Tai, N.-H.; Lin, I.-N. Nirogen-Incorporated Ultrananocrystalline Diamond Microstructures From Bias-Enhanced Microwave N_2/CH_4-Plasma Chemical Vapor Deposition. *Plasma Processes Polym.* **2016**, *13*, 419.

DOI: 10.1021/acsami.9b17942
ACS Appl. Mater. Interfaces 2019, 11, 48612−48623

(58) Saravanan, A.; Huang, B.-R.; Sankaran, K. J.; Kunuku, S.; Dong, C.-L.; Leou, K.-C.; Tai, N.-H.; Lin, I.-N. Bias-enhanced Nucleation and Growth Processes for Ultrananocrystalline Diamond Films in Ar/CH4 Plasma and Their Enhanced Plasma Illumination Properties. *ACS Appl. Mater. Interfaces* **2014**, *6*, 10566−10575.
(59) Butler, J. E.; Oleynik, I. A Mechanism for Crystal Twinning in the Growth of Diamond by Chemical Vapor Deposition. *Philos. Trans. R. Soc., A* **2008**, *366*, 295.
(60) Bogdanowicz, R.; Sobaszek, M.; Ryl, J.; Gnyba, M.; Ficek, M.; Gołuński, Ł.; Bock, W. J.; Śmietana, M.; Darowicki, K. Improved Surface Coverage of an Optical Fibre with Nanocrystalline Diamond by the Application of Dip-coating Seeding. *Diamond Relat. Mater.* **2015**, *55*, 52−63.

DOI: 10.1021/acsami.9b17942
ACS Appl. Mater. Interfaces 2019, 11, 48612−48623